ELSEVIER

Contents lists available at ScienceDirect

Surface Science

journal homepage: www.elsevier.com/locate/susc





Surface oxidation mechanism of CoCrFeNi high entropy alloy

Frank McKay^a, Timothy Ismael^{b,1}, Alexa Robinson^b, Orhan Kizilkaya^c, Phillip T. Sprunger^{a,*}, Pedro A Derosa^{b,*}

- ^a Department of Physics and Astronomy, Louisiana State University, Baton Rouge, LA 70803, USA
- ^b Institute for Micromanufacturing, Louisiana Tech University, Ruston, LA 71272, USA
- ^c Center for Advanced Microstructures and Devices, Louisiana State University, Baton Rouge, LA 70803, USA

ARTICLE INFO

Editor: Hans-Peter Steinrück

Keywords: High-entropy alloy Corrosion Density functional theory Photoemission Oxidation mechanism

ABSTRACT

High-entropy alloys (HEAs) are becoming increasingly important in advanced manufacturing applications due to their exceptional material properties, including oxidation resistance at and within extreme conditions. In this study, a combined experimental and theoretical approach is used to elucidate surface/near-surface details of structural, energetic, and chemical/electronic properties of CoCrFeNi, a quaternary fcc HEA, upon exposure to oxygen. Employing Density functional theory (DFT) calculation and DFT-driven Molecular Dynamics (DFT-MD), as well as photoelectron spectroscopy, we show strong evidence that, at the oxygen coverages used, oxidation is limited to the near-surface region of this random HEA and that the propensity of oxidation of $Cr >> Fe \approx Co >> Ni$ atoms, identified by an enhanced hybridization of the O 2p with the Cr 3d, and lesser extent to Fe and Co. Moreover, comparing to the O interaction strength in pure metal surfaces, there is weakening of Cr-O binding due to the presence of Co and Ni while Co-O binding is stronger. Ni-O does not seem to be affected, but being this the weakest interaction, O binds to Cr, Fe, and Co and little is left to bind with Ni.

1. Introduction

With the emergence of new advanced manufacturing and material fabrication techniques, High Entropy Alloys (HEAs) have gathered increased material attention due to the number of possible combinations of atomic elements and the flexibility associated with this diversity to optimize material properties for desired applications. [1-3] Conventional alloys are composed of a principal material (e.g. nickel-based superalloys and iron-based alloys) with additional elements in lower concentrations added to provide improved properties. [4,5] However the development of alloys with four or more principal elements in equimolar or near equimolar composition [5,6] has given rise to a new set of alloys with high configurational entropy with even more interesting properties. [7-9] Specifically, HEAs are becoming increasingly popular in manufacturing due to their excellent mechanical strength and their magnetic, electrical, and thermodynamic properties, which can vary greatly from one alloy composition to the next. Selective laser melting (SLM) (3D printing) is currently one of the most popular additive manufacturing methods and is suitable for the fabrication of HEA-based structures taking advantage of the HEA's distinctive

properties. [1]

Although major advancements in fabrication techniques and the improvement of alloy properties resulting from the development of HEAs has been achieved, there is still a need for further improvement. Zang *et al.* indicated that although achieving alloy density of 99.03%, 541.17 HV_{0.2} hardness and 162.1 MPa compressive strength, balling effects and residual stresses affecting the structure of the material still remain in the AlCoCuFeNi HEA during the SLM process. [10] In an investigation of the AlCoCuFeNiTi HEA as a wear resistant coating for high-velocity-oxygen-fuel thermal spray, Lobel *et al.* found that there was still some minor cracking and spallation in the alloy coating. [11] FeCoNiNb_{0.5}Mo_{0.5} and FeCoNiNb HEAs were studied by Tsau *et al.* as a replacement for the highly corrosion resistant FeCoNi alloy to obtain an alloy with greater indentation hardness, however, the increase in hardness of these two alloys compared to FeCoNi, was accompanied by a decrease in corrosion resistance. [12]

Several other studies on HEA properties have been conducted and yet limited information exists on oxidation mechanisms in these alloys. As HEAs become more popular, particularly for SLM, oxidation resistance becomes a critical property. The study of HEA's thermal properties is

^{*} Corresponding authors.

E-mail addresses: phils@lsu.edu (P.T. Sprunger), pderosa@latech.edu (P.A. Derosa).

¹ Currently at Department of Physics and Engineering Physics, Tulane, University, New Orleans, 70118.

often coupled with oxidation studies. [13,14] For example, studies of high temperature oxidation resistance of WMoCrTiAl, NbMoCrTiAl and TaMoCrTiAl HEAs at 1000 and 1100° C revealed that the oxidation resistance was best in TaMoCrTiAl due to a protective aluminum oxide scale that forms underneath a titanium oxide layer. The formation of a protective aluminum oxide layer was least likely in the WMoCrTiAl alloy due to the reaction between Al_2O_3 and WO_3 to form aluminum tungstate or $Al_2(WO_4)_3$. The NbMoCrTiAl HEA was found to have a high oxidation rate. Although a protective layer of Al_2O_3 does form, high amounts of oxygen and nitrogen were still able to dissolve in the alloy contributing to the presence of a thick internal corrosion layer in the NbMoCrTiAl alloy. [15]

A better understanding of the oxidation mechanism in these alloys can guide the selection of HEAs' composition that minimizes the effect of oxidation for the SLM approach to additive manufacturing. The alloy investigated in this study is composed of cobalt, chromium, iron, and nickel (CoCrFeNi) in equal atomic composition. CoCrFeNi has been reported by various researchers to have an *fcc* single-phase structure, [16, 17] with high tensile strength and ductility. [18] The nearest neighbor bond distance for such alloy surfaces is an average of 2.52 Å [16,18,19] with a lattice parameter of 3.55 Å. In this work, the oxidation mechanism in CoCrFeNi alloy is investigated to identify key atomistic details of the oxide formation on the surface using a combined technique of photoemission experiments and DFT calculations. Despite the surface being random and stoichiometric, as detailed below, our combined techniques both show that there is a heightened propensity of oxidation of Cr then Fe/Co, as compared to Ni.

2. Clean & oxidized surface

2.1. Methods - Experimental

High purity (> 99.9%) Co, Cr, Fe, and Ni with the same atomic percentage was arc melted into a pellet that was subsequently cut and polished with alumina down to 0.05 µm. The polished billet was then annealed at ~800°C in UHV conditions for a period of >24 hours to provide a more homogenous sample and minimize near-surface impurities. The resulting HEA homogeneous composition (1:1:1:1) was confirmed with Electron Backscattered Diffraction (EBSD) and Energy Dispersive X-ray Spectroscopy (EDS). The HEA lattice fcc structure has been calculated from X-ray Diffraction (XRD) to be a = 3.56 Å. All X-ray Photoelectron Spectroscopy (XPS) and Ultraviolet Photoelectron Spectroscopy (UPS) experiments were performed in ultra-high vacuum chambers ($< 3 \times 10^{-10}$ Torr) and the HEA crystalline surface ($\sim 1 \text{cm}^2$) prepared by cycles of ion sputtering (5×10⁻⁵ Ne; 2 keV; 45 min) and subsequent annealing to 800°C (15 min), which resulted in a clean surface. Subsequent angle-resolved photoemission measurements were performed using 1.3 GeV synchrotron light at the 5m-TGM beamline [20] at LSU's Center for Advanced Microstructures and Devices (CAMD) in normal emission geometry and 80 eV photon energy. In addition to low-energy electron diffraction (LEED) experiments, XPS experiments were performed with both a Specs Phoibos 150 Electron Analyzer with a monochromated Al K α X-ray ($\hbar\omega=1487$ eV) source and an Omicron EA 125 hemispherical electron energy analyzer with a Mg K α X-ray ($\hbar\omega=$ 1254 eV) source. HEA oxygen adsorption was performed via a leak valve $(\sim 0.1-2\times 10^{-6} \text{ Torr O}_2)$ onto the room temperature sample.

2.2. Methods - Computational

To simulate this CoCrFeNi alloy that was manufactured, 4 atomic layers thick slabs were created with the same number of atoms of each element that were randomly distributed in the volume to ensure that sample slabs are statistically independent from each other. Two different slab sizes were created for the different parts of the study, a larger slab, with 168 atoms total (42 of each element) and a smaller one with 100 atoms (25 of each element). Upon creation, the distribution of the

different metallic atoms in each slab was further checked to ensure the distribution is closely uniform throughout the sample. This extra further step was deemed necessary because the small size of the sample makes the probability that a group of atoms of the same element end up placed close together large enough to be a problem. However, only extreme cases were eliminated. Periodic boundary conditions in the three dimensions were applied with a 20 Å vacuum layer in the direction perpendicular to the surface. The vacuum layer is introduced to avoid the interaction of the layer with its own image above and below.

The samples were built and optimized using Atomistix ToolKit (ATK) v2017.12 atomic modeling software. [21] The CoCrFeNi alloy surfaces were optimized via spin-polarized DFT calculations using the Spin-polarized generalized gradient approximation with the Perdew, Burke and Ernzerhof exchange-correlation functional (GGA-PBE). [22] This method was also employed by Middleburgh *et al.* [16] for a similar system and by Zhang *et al.* [23] for calculations on some CoCrFeNi-based alloys. A Double Zeta Polarized basis set [24,25] was used. The sampling of the Brillouin zone was conducted using a $1 \times 5 \times 5$ k-points grid, with a density mesh cutoff of 13,605.7eV. The Self-consistent field (SCF) iterations tolerance was set to 10^{-4} . The Geometry Optimization method used was the Limited memory Broyden–Fletcher–Goldfarb–Shanno (LBFGS) [26,27] with a force tolerance of 0.05eV/Å.

DFT-MD simulations were conducted using the Nose-Hoover NVT ensemble with a 300K target temperature and a 2 fs time step. The DFT parameters assigned were the same as described above.

The binding energy for oxygen adsorption on the surfaces was calculated using the following equation:

$$BE = E(slab + O) - E(slab) - \frac{E(O_2)}{2}$$
(1)

where $\frac{E(O_2)}{2}$ is half the calculated energy of the oxygen molecule, E(slab + O) is the total energy of the slab with an oxygen atom adsorbed, and E(slab) is the total energy of the bare slab. In Eq. (1), $\frac{E(O_2)}{2}$ was used as opposed to E(O) in order to refer the binding energy to the O molecule and not to the atomic form of O. Thus, Eq. (1) is the difference between the energy of an oxygen atom adsorbed on the slab and the energy of the bare slab plus the energy of the oxygen molecule per atom.

3. Clean & bulk surface properties

3.1. Experimental

To experimentally probe the spatial compositional homogeneity of the surface, EBSD and EDS measurements on a freshly polished and annealed sample were performed. Fig. 1 shows an EBSD image across a portion of the sample. This confirms that our sample contains large crystal domains of $100-1000\ \mu m$ in size.

In addition to the above EBSD image, four EDS images of the sample can be seen in Fig. 2. EDS shows the elemental distribution of the four component elements of this HEA sample. No evidence of preferential elemental segregation in the near-surface region (down to $\sim\!10$ nm) is observed.

3.2. Computation

Computationally, the structures before (left) and after (right) geometry optimization for the three large CoCrFeNi HEA slabs shown in Fig. 3. All slabs were created with an equal number of each atomic element. This is consistent with previous angle-dependent XPS data, [28] which revealed nearly equal concentrations of each constituent metal in the near-surface region (both on clean and oxidized surfaces). An *fcc* lattice structure was chosen because the structure for CoCrFeNi has been reported to have an *fcc* single-phase structure [17] and confirmed for the structures experimentally studied here. The surface was cleaved across the (111) crystal orientation. In a polycrystalline



Fig. 1. EBSD image of CoCrFeNi HEA sample at 500 µm scale bar. Inset (bottom left) shows the color scale of (fcc) crystal grain orientation.

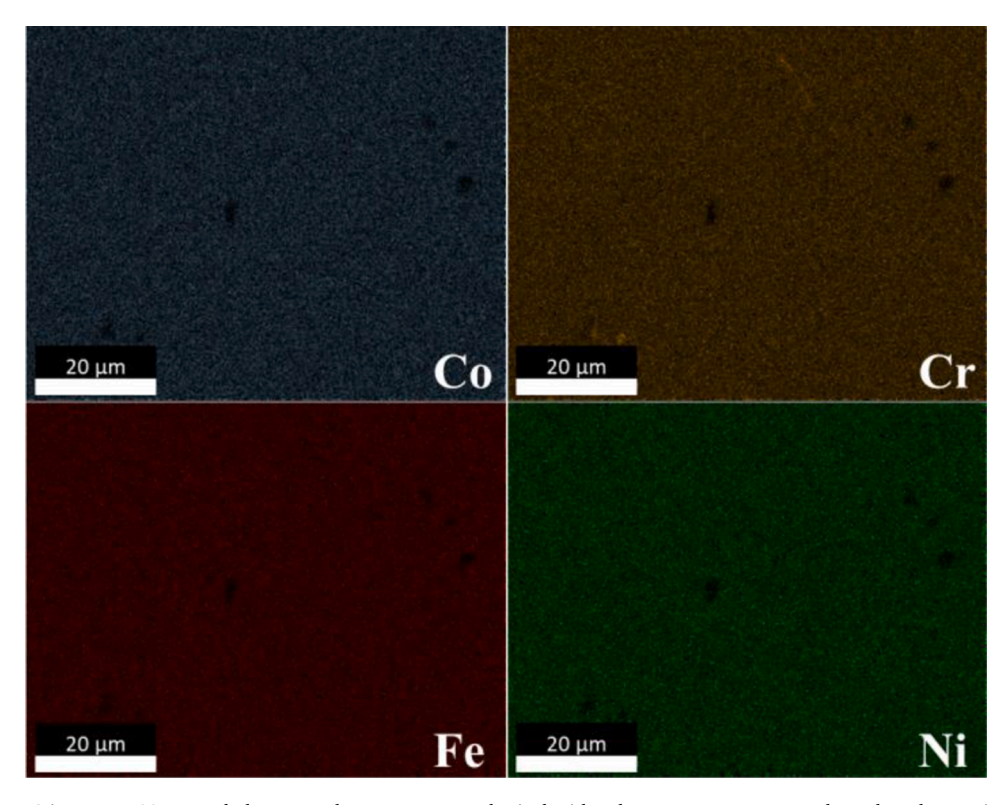


Fig. 2. EDS images at 20 μm scale bar, over the same area. Each pixel with color represents an area where that element is present.

sample, different orientations are possible and there is no one orientation that is preferred over the others. Considering that large number of atomic configurations that are possible for each surface orientation, one orientation, the (111), was selected for this study. The nearest neighbor bond distance for this optimized surface is an average of 2.52 Å, that is, a lattice parameter a=3.56 Å. This agrees with the structures in the experiments reported here, but also with the reported value for this alloy

(a=3.55 Å) [20,23,24], from which the nearest neighbor distance of 2.51 Å is calculated. Similar results were obtained for three statistically independent, random surface models shown in Fig. 3.

In the optimized structures, it is observed that Cr atoms in the outer layers, relax perpendicularly outwards more than atoms of the other elements. In Fig. 3, using the horizontal as a reference, it can be seen how Cr atoms stick out compared to the rest of the elements in all the

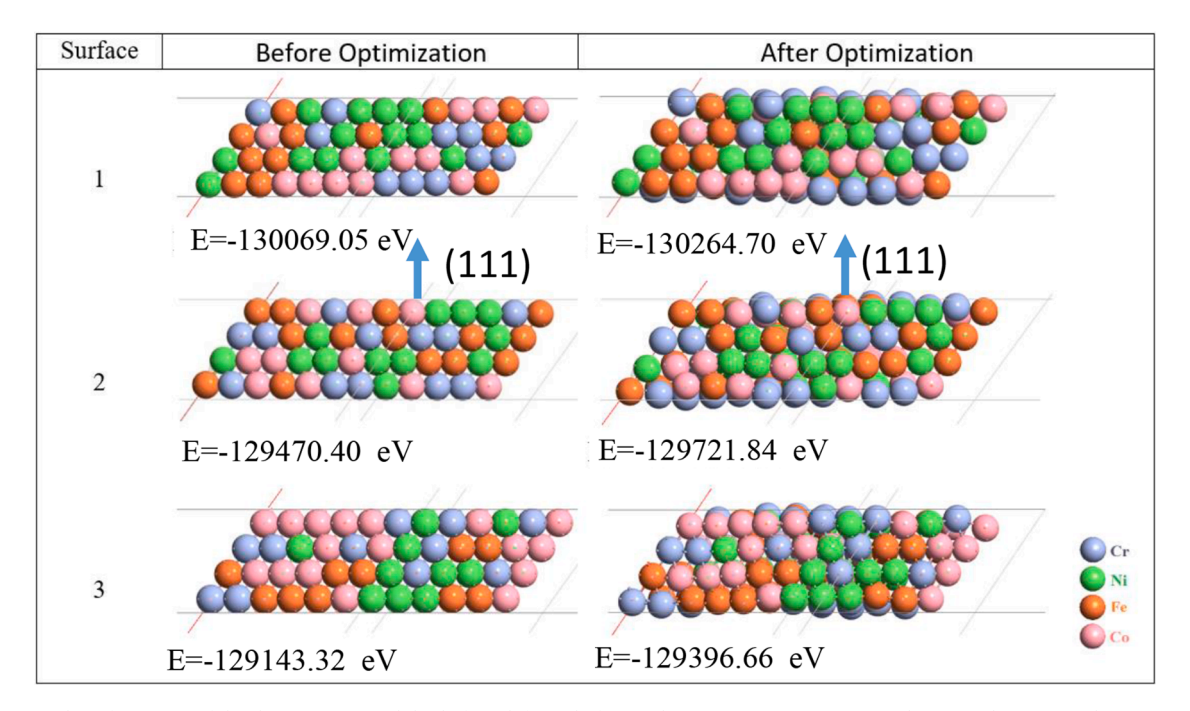


Fig. 3. Geometrical configuration of the three 168-atom slides before (left) and after (right) geometry optimization. The (111) direction is shown in surface 2. The orientation is the same for the other two slabs.

slabs. Cr has been observed to migrate to inter-dendritic regions and to the surface of the alloy as previously reported by Qiu et al [29] while investigating the segregation and migration of constituent elements in the CoCrFeNi HEA. This migration was attributed to Cr magnetic moment, however, the simulation times that are currently possible for these types of simulations are not nearly long enough to consider this evidence of segregation. Furthermore, the Magnetic Moment of Cr is antiparallel to that of Fe, Co, and Ni [17, 23]what according to Middlegurgh et al. [16] leads to a stabilization or trapping of Cr in the HEA structure, which is consistent with experimental observations reported here, and therefore, the tendency of surface Cr to optimize further out than other elements is only mentioned here because it is consistent in all simulations, but no claim of Cr segregation is made. The energy of the optimized surface is, in all slabs, between 9 and 10 Ha lower than in the initial configuration where atoms are in a perfect fcc configuration.

4. Oxygen adsorption

4.1. Photoemission Experiments

To experimentally probe the CoCrFeNi alloy's reaction to O_2 , a clean (sputtered and annealed) sample was exposed to increasing amounts of O_2 . XPS spectra of a sample before and after exposure of $1000L\ O_2$ can be seen in Fig. 4. The spectra of a clean sample show the characteristic $2p_{1/2}$ and $2p_{3/2}$ features of the various metals. [30] Additional features appear at higher binding energies for spectra of a dosed sample, which indicate the formation of oxides. [30]

For each of the clean surface spectra, the area attributed to the $2p_{3/2}$ metal peak was fit using the commercial software CasaXPS [31] following the removal of the secondary electron background using a standard Shirley method. [32] For the data taken following O_2 exposure, the spectra were fit with this same metal peak, with Doniach-Sunjic line-shape, [33] using the same binding energy and width (FWHM) as spectra of a clean sample. Due to interference from Co LMM Auger peak, data from Mg K α X-ray source ($h\omega=1254$ eV) was used. Additional peaks were then fit to the spectrum to represent the contribution of the oxides to the spectra (see Cr fit in Fig. 4). Fig. 5 shows a plot of the areas obtained by this fitting procedure as a function of O_2 exposure for each

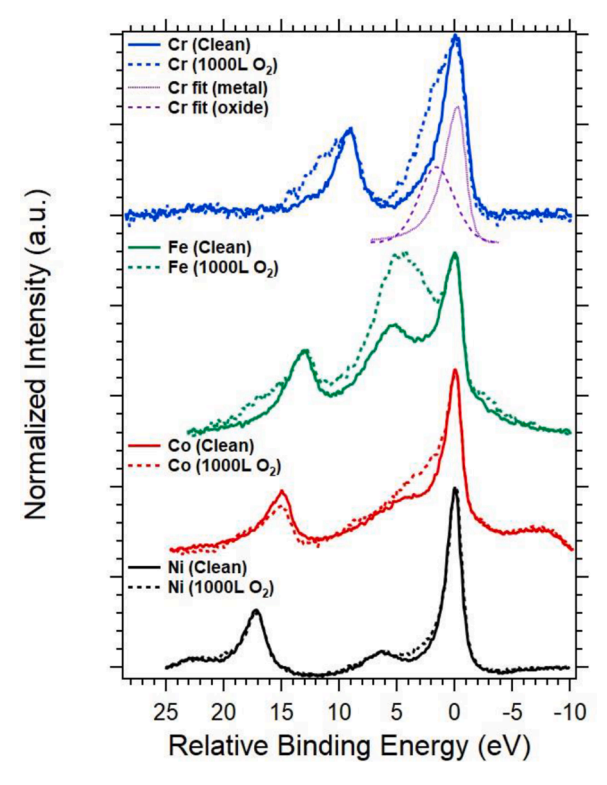


Fig. 4. XPS spectra ($\hbar\omega=1487$ eV) of all four metal peaks before (solid line) and after (dashed line) exposure to 1000L of O_2 . Binding energy of all spectra have been shifted (from Cr=574.2 eV, Fe=706.6 eV, Co=778.1 eV, and Ni=852.6 eV to zero) so that zero relative binding energy corresponds to the location of the primary $2p_{3/2}$ peak of each metal. Peak in Fe spectra ~ 6 eV above Fe $2p_{3/2}$ due to Co LMM Auger peak.

of the metals, which represents the increase in surface oxide coverage as a function of oxygen exposure. The data are plotted as a ratio of the areas of the oxide-related $2p_{3/2}$ features to the areas from the $2p_{3/2}$ metal

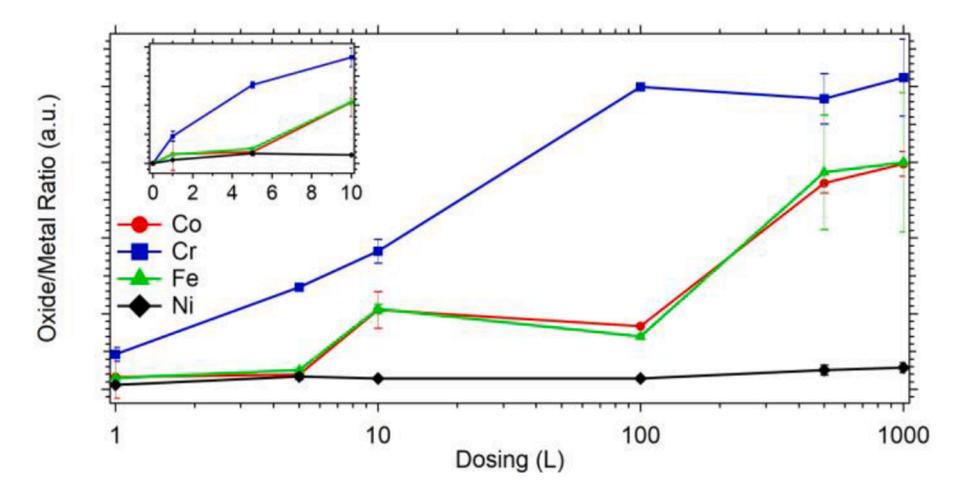


Fig. 5. Area of the oxides peak to the area of the metal peak as fitted by CasaXPS as a function of O₂ dosage from 1L to 1000L O₂. Inset shows this same ratio on a linear scale from clean (0) to 10L O₂.

components. The result provides insight into the onset of oxidation as well as the exposure needed to saturate each oxide component on the surface.

It can be seen in Fig. 5 that the formation of Cr oxides happens quickly (within 5 L O_2) and saturates below 100 L O_2 , with little change in the oxide ratio for exposures beyond that point. Fe and Co are next to oxidize, with saturation occurring around 500 L O_2 . While there is a small change in the oxide ratio for Ni, it can be seen from Fig. 4 that there is no shift in the position $2p_{3/2}$ peak of Ni even at $1,000 \text{ L O}_2$, which would be expected if no Ni oxides were formed. Moreover, there is no discernable indication of a characteristic NiO shake-up at 861 eV [34] even at $1,000 \text{ L O}_2$, while there is persistence of the metallic shake-up at 858 eV binding energy.

4.2. Computational Modeling of the Oxidation Process

To better understand the initial stages of the oxide formation in the CoCrFeNi alloy density, oxygen atoms were initially positioned uniformly about 3\AA above the geometry-optimized 168-atom slabs and subjected to DFT-MD simulations. The results of these simulations are shown in Fig. 6 where the initial geometry (a,b) and the geometry after

4.2 ps, when the equilibrium temperature has already been reached (c, d), are depicted for one of the surface models. The position of the oxygen atoms on the (111) exposed surface is displayed using top (a, c) and side (b, d) views. The simulation box in Fig. 6 contains 15 O atoms on a 168 atom CoCrFeNi surface. Once thermal equilibrium is reached, the alloys is found to still be in an fcc crystal structure with an average nearest neighbor distance around 2.5Å. The increasing degree of disorder observed in the calculated structure shown in Fig 6 are confirmed experimentally with LEED (see Figure S1 in Supplemental Information). The local surface crystalline structure, as revealed by the degradation of the sharp LEED patterns (averaging over multiple domain structure), is nearly absent by exposure of 100L O₂.

A trend where O preferentially associates with Cr is observed from these simulations. To quantify the observations, the average distance between each metal atom and all O atoms within a 4 Å radius of it, was calculated. The result was then subtracted from a hypothetical uniform distribution of atoms. From the initial configuration, at t=0, where O atoms are uniformly distributed, the calculation is repeated at each time step of the simulation. In other words, this is an indication of how much closer or further from each metal element O is when the O atoms are distributed as predicted by the simulation than for a random distribution

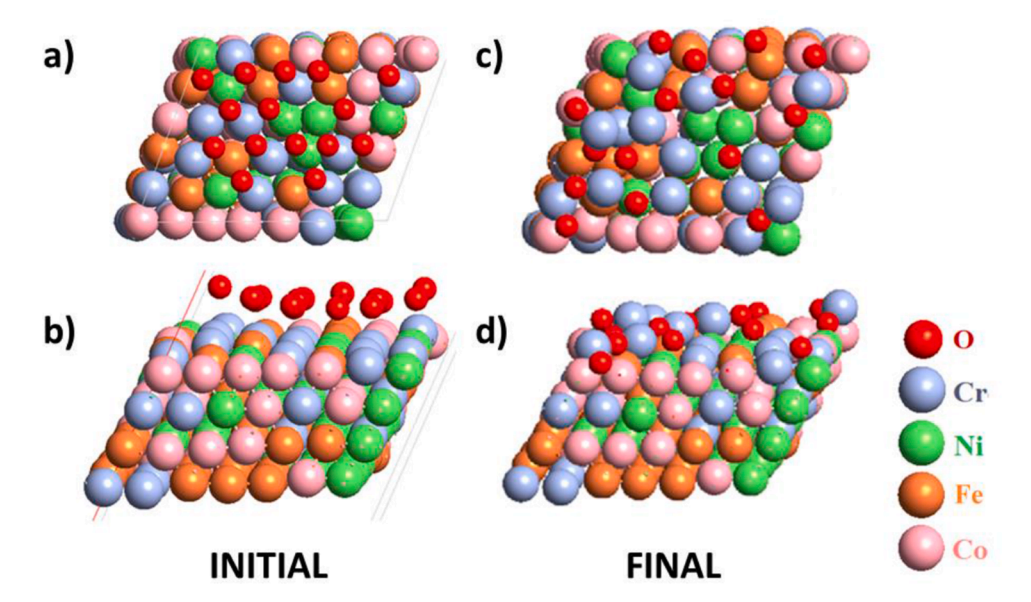


Fig. 6. CoCrFeNi surface model exposed to a layer of O atoms positioned above the exposed (111) surface. a) top view and b) side view of the initial configuration. C) top view and d) side view of the configuration after 4.2 ps of DFT/MD.

where the position of the O atoms is not biased by their affinity to any particular elements. A running block average in 120 fs blocks is used to smooth out the thermal oscillations around an equilibrium position. Results are shown for one of the slabs in Fig. 7. The average metal-O distance is observed to decrease for Cr and Fe and increase for Co and Ni. The tendency of O to move towards Cr is quite clear from these results. This trend is observed in all the slabs simulated here. These results sugges that, in order of preference, O will migrate towards Cr. In addition, O is also found slightly closer to Fe and slightly further from Co, while it is clearly moving away from Ni.

As mentioned above, during the equilibration period, oxygen atoms migrate towards Cr and Fe rich sites and remain in close proximity to the aforementioned sites after equilibration and for the duration of the simulation as shown by the position of the O atoms in Figure 6c and d. This agrees with XPS measurements (figures 4 and 5) that show that Cr tends to be oxidized first, followed by Fe and Co.

With a better understanding of O adsorption trends, smaller models (100 atoms) of the surface slab, containing 25 atoms of each element, were built. The 100-atom CoCrFeNi, periodic slabs were optimized via DFT using the aforementioned method and parameters. An O atom was initially placed 3Å above the surface at a selected position and the systems re-optimized. This step was repeated, placing the O atom in a different location each time to obtain adsorption at all possible hollow sites and bridge sites. Hollow-site adsorption was more favorable than at bridge-sites for individual atoms; in fact, most of the bridge-site's locations proved to be unstable and the O atom did not stay there after optimization. Only the Fe₂, CoFe, and CoNi bridge-sites were successfully obtained. An example of O adsorption at a hollow (NiFeCr) and a bridge (Fe₂) adsorption site are shown in Fig. 8(a) and (b), respectively.

The average binding energy of individual O atoms at various hollow and bridge sites is shown in Fig. 9 as a function of the average atomic number (Z_{avg}), which increases with the d-band filling of the 3d metals, of the atoms composing the adsorption site. The average as opposed to the sum of atomic numbers was used so that hollow and bridge sites can be directly compared in the same plot. The general trend shows that binding energy decreases with the increase in Z_{avg} , this translates to a preferential binding to Cr, followed by Fe, Co, and Ni, at least from the energetic point of view. A similar relationship between the differential reduction free energy of adsorbed atomic oxygen in CoCrFeNi and the atomic number of the atoms in the site has been seen by McKay $et\ al.$

It is surprising that, although the bridge site was found unstable in general, the ones that converged to a stable configuration (Fe-Fe, Fe-Co, and Co-Ni) seem to have a higher BE than hollow sites with similar Z_{avy} ,

however, while the average for all the reported hollow sites (except CrFeNi and CrCoNi) includes 5 different sites in three different slabs, not many bridge sites were found stable. For the Fe-Fe and the Co-Ni bridge site, only one configuration converged while 3 configurations converged for the Fe-Co bridge site. Nevertheless, the trend is observed among bridge sites as well, with Fe-Fe providing the highest BE followed by Fe-Co, and a much smaller binding energy for Co-Ni.

It was not possible to obtain binding energies for adsorption at two of the four possible hollow sites made up of atoms from 3 different elements, namely sites CrCoFe and CoFeNi and for a third one, CrCoNi, the binding energy was obtained for 3 different sites in two of the three surfaces. The reason is that binding energy to these sites is low and the O atom is observed to migrate away from these sites. This reveals that three unique-element sites tend to be unfavorable for binding. In general, however, Cr-rich sites have a higher binding energy than Fe-rich sites followed by Co and least at Ni-rich sites indicating the preference in oxide formation on the CoCrFeNi HEA surface. This again agrees with our previous computational and experimental observations.

The binding energy for O on pure metal slabs is also displayed in Fig. 9 (blue diamonds). The first observation is that the trend is inherent to the metal themselves as it is followed in pure metal surfaces. It is however interesting to note that the interaction between Cr and Fe with O is weakened when these metals are in the HEA compared with their interaction as pure metals while the interaction with Co is stronger in the HEA and the Co metal. The interaction between O and Ni is only mildly increased.

5. Surface electronic properties

5.1. Partial Density of States

The projected density of state (PDOS) was calculated for the CoCr-FeNi (111) surface with one O adsorbed at different sites. Fig. 10 shows the PDOS for O at (a) $\rm Cr_3$ (c) $\rm Cr$ -Cr-Ni and (e) $\rm Cr$ -Fe-Ni hollow sites with the sites shown in (b), (d) and (f) respectively. These sites were selected as they have a decreasing number of Cr atoms, with Ni in the second site and Fe-Ni in the third. The effect of the presence of Cr and Ni will give insight of the effect one atom has on the other. Since interaction between the O 2p and metal 3d orbitals is expected for the oxide formation in the alloy (as evidenced by the hybrid states in the photoemission spectrum in Fig. 4), the DOS was projected over the p orbitals of the O atoms and the 3d orbitals of each of the metal atoms in each site. These states are shown with respect to the Fermi energy for a -10.0eV to 1.0 eV range.

For the O atom adsorbed at the hollow sites (see Fig. 10), a region of

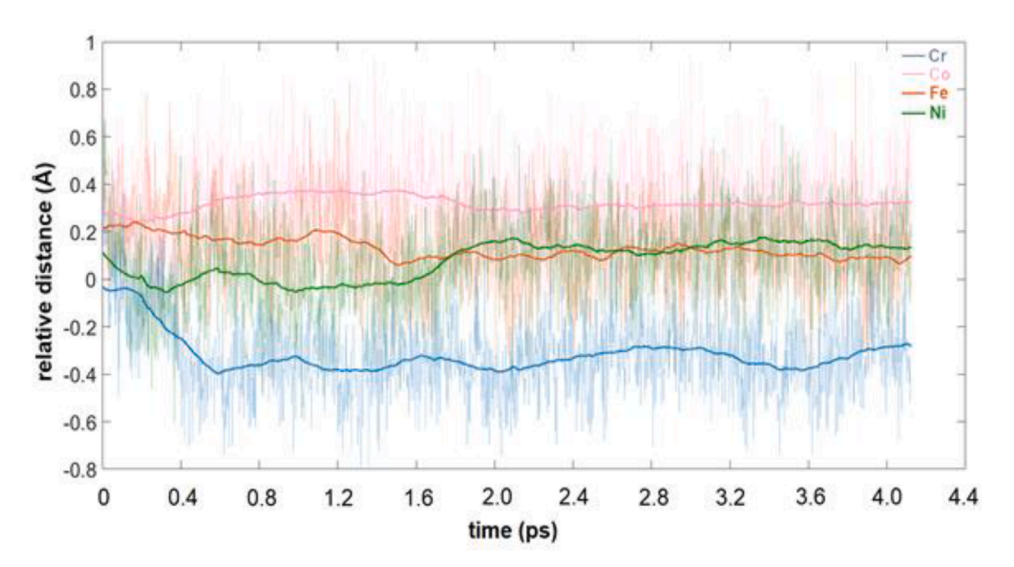


Fig. 7. Evolution of average oxygen to element distance throughout the DFT-MD simulation.

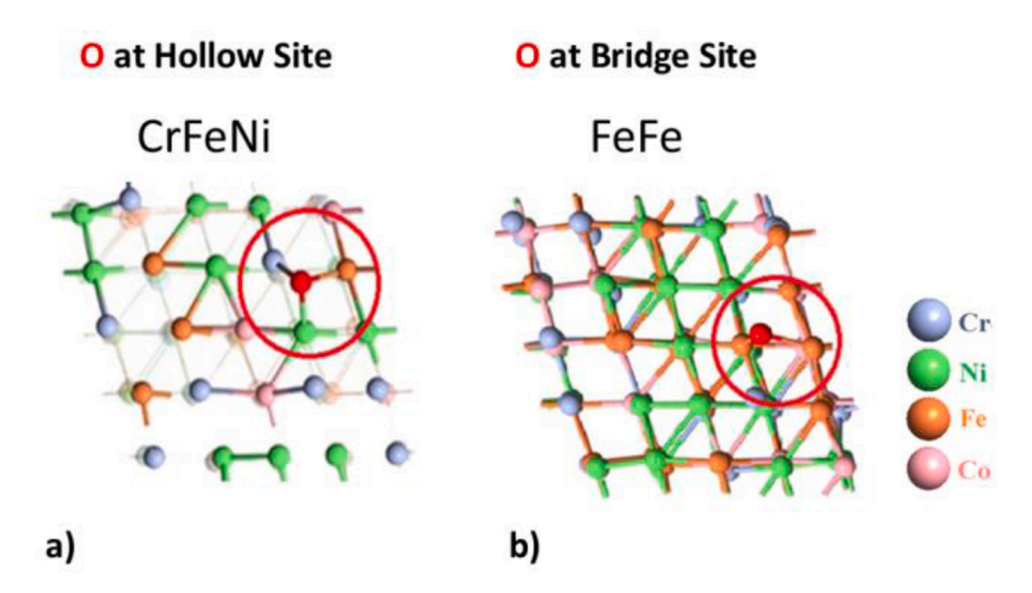


Fig. 8. Oxygen adsorption at the surface, a) at a CrFeNi hollow site and b) at a Fe2 bridge sites.

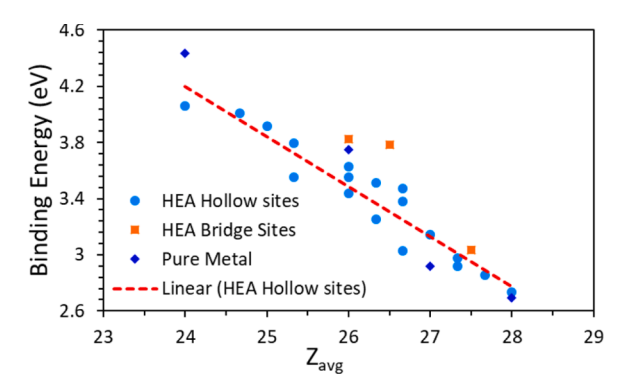


Fig. 9. Calculated binding energy for oxygen adsorbed at various hollow and bridge sites averaged for three statistically independent surfaces. The blue diamond show the binding energy to the corresponding pure metals.

high density of states for the O 2p orbital is identified within the -6 to -4 eV energy range. A similar finding is reported by Li et al. [35] while investigating oxygen adsorption on Ag (111) surface. Within the same energy range, there is a peak in the PDOS for Cr 3d, which is almost identical for the three atoms in the site. This indicates the probability of bond formation between O and Cr. For the Cr3 site (Figure 10a and b), a similar density is observed for all the three Cr atoms suggesting a similar bond order for all the three atoms. This is confirmed by the analysis of the molecular orbitals (MOs) obtained through molecular energy spectrum calculations. In each of the cases, three orbital energies are obtained within this energy range and the energies are represented by the three vertical lines, labeled 1, 2 and 3 in the PDOS plots. From the shape of the MOs (Fig. 10b), it is clear that each of these are associated with one of the p levels of O that allows for even hybridization with all the three Cr atoms. Orbital 1 is associated with p_z (arbitrarily aligning the z axis perpendicular to the plane of this hollow site) while the other two are related with p_x and p_y . It is noted that the three MOs are roughly equally delocalized between the O and the three Cr atoms and it is expected that the O will be similarly bonded to the three Cr atoms indicating a high probability of chromium oxide formation at that site. Certainly, since the most common form of this oxide is Cr₂O₃, it is not possible to observe its formation with these calculations where only one O atoms is present on the surface.

Results for the adsorption of O at a Cr_2Ni site are recorded in Fig. 10c) and d). The PDOS for the Cr 3d orbitals show an uneven

distribution. For Cr(91), the PDOS is greater than for Cr(11) and Ni, hinting that the binding to the three atoms in the hollow site is not equally strong. This is shown in the inset in Fig. 10(c). The corresponding orbitals for the three energy levels identified in this range are shown in Fig. 10(d). MO 1 bonds Cr(91) and Ni, while MOs 2 and 3 both show binding between the O and the two Cr atoms, but not with Ni.

At a CrFeNi hollow site, shown in (e) of Fig. 10, the PDOS for the Cr, Fe and Ni atom 3d orbitals reveals a greater density of electronic states for the Fe 3d orbitals than the Cr and Ni. The overall picture shows a stronger bond to Fe. MO 1 shows O simultaneously binding to Fe and Ni, however, MO 2 and 3 are mostly FeO with a mild binding to Cr in MO 3.

To further understand the complex interaction between the different metals on the HEA, the projected density of state (PDOS) is shown in Figures S2, S3, S4, and S5 (in Supplemental Information) for O at Cr-Cr-Ni, Cr-Ni-Ni, Cr-Co-Co, and a Cr-Fe-Fe sites, respectively. For a Cr-Cr-Ni site (Figure S2), the electronic distribution of the three crystal orbitals shows mostly contributions from Cr and O, while for a Cr-Ni-Ni site (Figure S3), the electronic distribution is more even allowing O to bond to Ni as well as Cr. Moreover, comparing the Cr-Ni-Ni (Figure S3) and Cr-Co-Co (Figure S4), it can be seen that the crystal orbitals evidence a stronger interaction between O and the Co atoms than with Cr showing that in sites where Cr is the minority (Cr-Ni Ni and Cr-Co-Co) while Co is able to take O away from Cr, Ni shares it equally. Similarly, in a Cr-Fe-Fe site (Figure S5), although a little less obvious for surface 3, crystal orbitals bear a larger contribution from both Fe atoms than from the Cr atom in their interaction with O.

From this analysis, we can further understand what was reported above when looking at the binding energy data (Fig. 9), when Co or Fe are in a site with Cr, they lower the ability of Cr to bond to O compared to its interaction in a pure Cr surface. Ni seems to be more inert and neither affect nor be affected by other elements. As described earlier, due to its magnetic moment being opposite to that of Fe, Co, and Ni, Cr does not segregate to the surface and thus it competes with other elements at each site for O. It is also evident from results reported here that its reactivity is not improved by the presence of the other elements, furthermore, it is weakened, therefore, the preferential binding order (Cr→Fe→Co→Ni) is not a new phenomenon caused by intermetallic interaction in the HEA, it rather simply follows the binding strength each of these metals show when in pure form (see dark blue rhombus in Fig. 9). What is interesting to notice, however, is that the interaction between elements leads to a weakening of the Cr-O and Fe-O interaction, a strengthening of the Co-O interaction, and has little effect on Ni (compare the dark-blue rhombus with the light blue circles). The fact

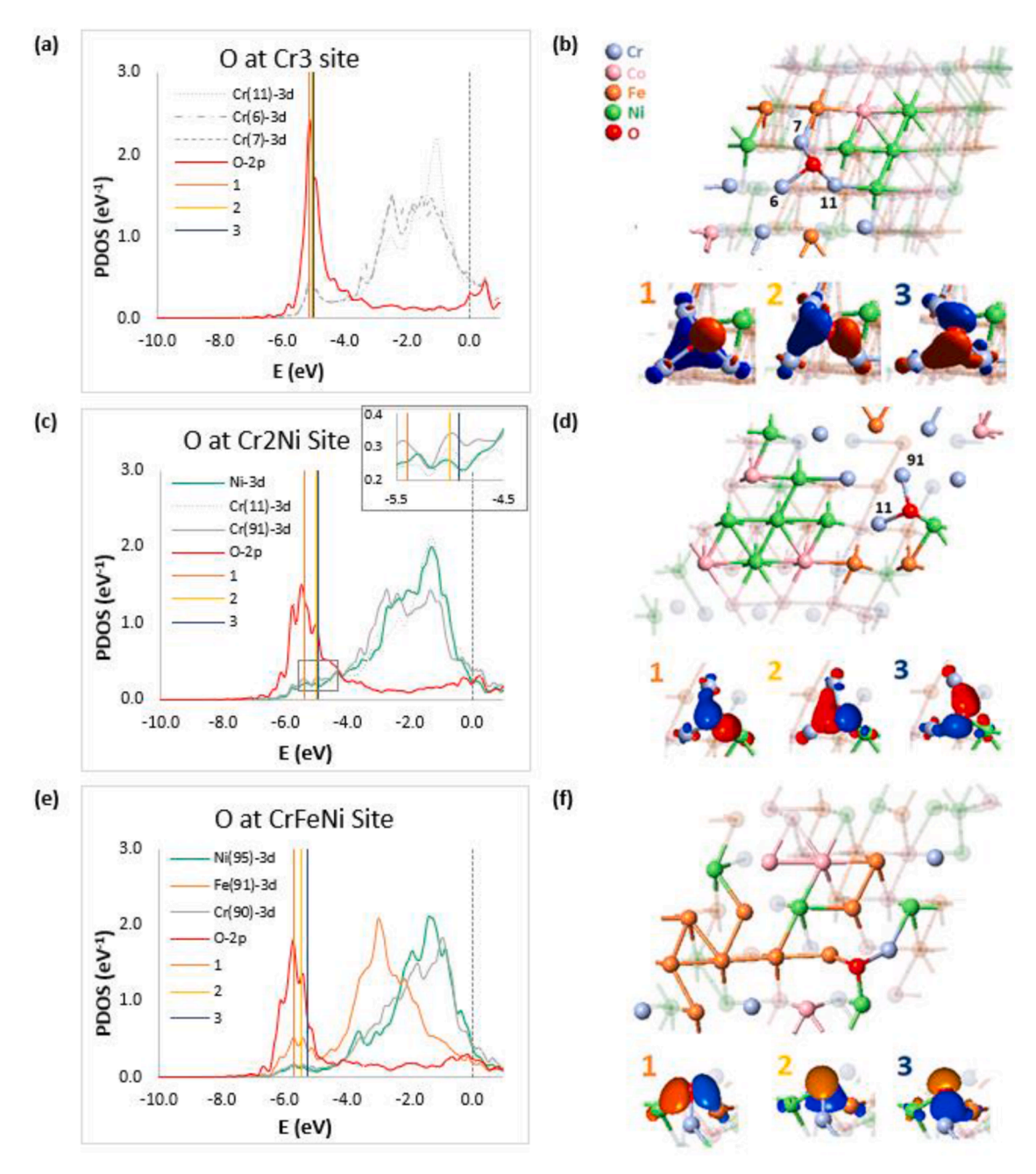


Fig. 10. Projected density of states for the O/CoCrFeNi (111) surface with O adsorbed at (a) Cr-Cr-Cr (c) Cr-Cr-Ni and Cr-Fe-Ni hollow sites respectively. Orbitals for the energy levels available within the high density of O_2p are shown in (b), (d) and (f) for the each of the three sites respectively (note that the inset showing the MO is rotated with respect to the orientation of this site in the surface right above). The energy levels are represented by vertical bars labeled 1, 2 and 3 in PDOS plots.

that Ni shows little to no oxidation is then not due to a weakening of its interaction with O due to the other elements, but seems to be due to two other factors. First, the Ni-O binding energy is already the smallest of all, as a result, when the oxidation starts, other elements oxidize first. Second, the elements in the HEA are almost uniformly distributed; therefore, Ni will be closely surrounded by sites with other elements that will already have O leaving little room for O to reach the remaining Ni sites.

5.2. UPS/PDOS Comparison

To provide a comparison between experimental measurements and computation of the density of states, PDOS of one full monolayer of O adsorbed on this surface was calculated while UPS experiments were conducted on this sample. The PDOS was calculated for O adsorbed on the surface projected over the p orbitals of all O atoms and the 3d orbitals

of all metals on the first and second atomic layers in the slab. The results from 3 different 100 atom surfaces were averaged. The overall PDOS contribution from each layer was scaled separately to consider the inelastic mean free path of photoelectrons resulting from UPS measurements (at $\hbar\omega=80$ eV). Only two layers were considered, the first (surface) layer was not scaled while the second layer was scaled by 0.554, which is the negative exponential of the nearest neighbor distance (2.52 Å) over the inelastic mean free path at 80 eV (4.27 Å). [36] This was done to account for the reduction in measured intensity of UPS spectra due to inelastic scattering. In addition, the data from the PDOS calculation was convoluted with a fermi-dirac function with a kT value of 0.1 eV, to simulate the resolution obtained from UPS measurements.

The results are plotted along with results of UPS spectra taken on a sample exposed to 100L of oxygen (Fig. 11). All UPS measurements were taken at photon energy ($\hbar\omega$) of 80 eV. A standard Shirley background

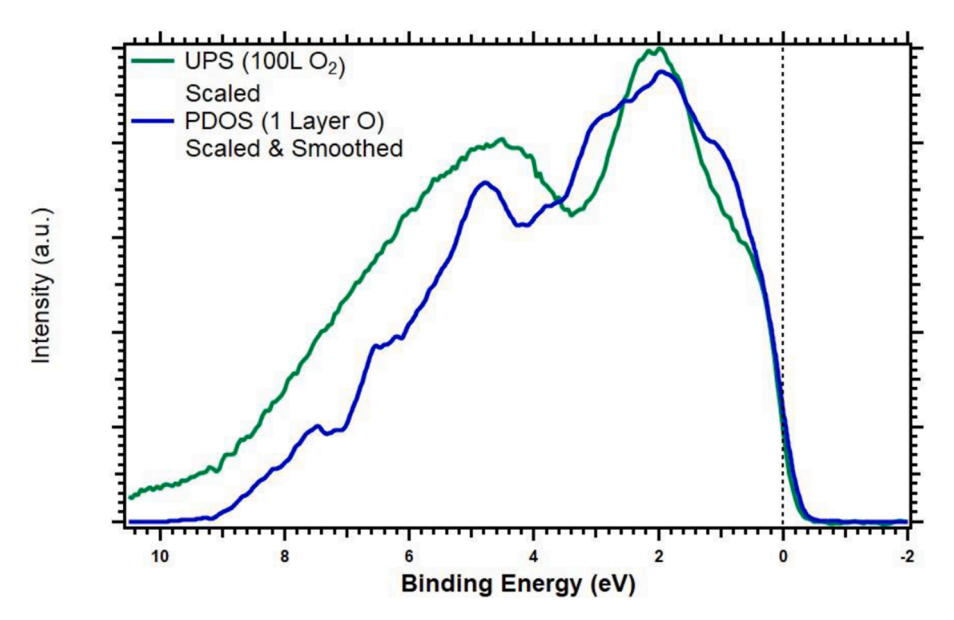


Fig. 11. Results of UPS spectra (green) of an oxidized sample can be compared to the total PDOS (blue) calculated. Vertical line indicates fermi-energy (E_f).

[32] has been applied and subtracted from the UPS results. The Fermi energy (E_f) has been determined by comparing measurements to gold foil spectra at the same photon energy. In both the UPS and PDOS of Fig. 11, distinct matching features can be seen. The contribution to the spectra up to 1.5 eV above E_f are the remnants of metallic (un-oxidized) 3d bands. While those features from 2-4 eV are due to hybridized states, the broad feature from 4-6 eV is due to O 2p bands. [37–40] As seen in Fig. 11, there is good agreement between experiment and theory giving credence to the overall understanding of the atomistic details of the oxidation mechanism of this HEA surface.

6. Conclusions

In this work, a computational study of the oxidation mechanisms in CoCrFeNi HEA is compared to experimental photoemission studies. The focus was on the initial stage of oxidation with the aim of identifying the mechanism, or preference and sequence, of oxide formation on the HEA surface. Four-layer CoCrFeNi slabs were examined through atomistic modeling. Experimentally a comparison was made through photoemissions studies after controlled exposure to $\rm O_2$ on a clean crystalline surface.

DFT Geometry optimization of clean 168 atom CoCrFeNi surfaces with (111) surface exposed showed that fcc lattice structure is stable and that the optimized structural parameters, with an average nearest neighbor distance of 2.52 Å, consistent with a lattice constant of 3.53 Å, agree with experimental data. Experimental characterization data (XRD/EBSD/EDS) confirms a homogeneous HEA sample, consistent with our computational setup.

DFT/MD revealed that oxygen preferentially adsorbs at Cr- and in less extent to Fe-rich sites. The oxygen atoms migrated from their initial, random, distribution towards Cr-rich and Fe-rich sites and away from Ni-rich sites. O remains in close proximity to the Cr and Fe sites after equilibration. Quantification of the observation showed that over the duration of the simulation, the Cr-O and Fe-O distance decreased and remained the shortest, confirming the preference of chromium oxide formation while oxygen tends to move away from Ni and Co. The presence of the oxygen layer did not affect the metallic crystal structure that was found to be in the *fcc* near-configuration at equilibrium with an average nearest neighbor distance of 2.52 Å.

The binding affinity of oxygen to the surface at hollow sites conformed by 3 atoms was found to be $\rm Cr > \rm Fe > \rm Co > \rm Ni.$ This was experimentally confirmed with analysis of the growth of oxide related

features to overall XPS spectra after increasing oxygen exposure. While surface oxidation of Cr is observed to saturate by exposure of less than 100 L, and Co and Fe by 1000 L of O_2 at RT, surface Ni remains unoxidized. For O adsorbed at a hollow site on the pure Cr or Fe surfaces, the binding energy is larger than that of O adsorbed in a HEA Cr_3 or Fe_3 hollow site respectively due to the presence other atomic species, particularly Co. On the other hand, the binding energy for O adsorbed at Co_3 in the HEA is slightly higher than on the pure surface. Ni seems to have less interaction with other metals.

The O binding energy at multiple element hollow sites shows the same trend where O prefers Cr over Fe, then Co and is lowest for Ni. However, a competition between Fe and Cr seems to occur. Although the binding energy in general decreases when the content of Cr at the site decreases, when Fe is in place, the MOs seem to suggest a larger binding tendency towards Fe than Cr. This is also observed when Co is in competition with Cr and explains that while the O binding energy to a single element hollow is lower in the HEA than in pure for Cr and Fe, but it is larger for Co.

Further MO analysis need to be conducted where more than one O atom is placed at the same time to allow the formation of other oxide forms, particularly $\rm Cr_2O_3$, which is the preferred form of oxide for Cr. Since in the calculations reported here, only one O atom is present on the surface, the only possible oxides are CrO and FeO. Since the latter is the preferred form of oxide for Fe, it is not surprising to see a strong competition between Fe and Cr. DFT/MD calculations on this HEA with multiple O atoms on top seem to confirm this, as some of the surfaces show what seems to be $\rm Cr_2O_3$.

Three-element sites are unfavorable for O adsorption with the exception of the Cr-Fe-Ni site, which was among the most favorable. The binding energy for this site was more favorable than the Fe₂Co, Fe₂Ni, Co₂Cr and Co₂Fe sites as well as the Co₃ and Ni₃ sites. In general, Cr-rich sites have a higher binding energy than Fe-rich sites followed by Co and then Ni-rich sites. On the contrary, the presence of Co or Ni at a site seem to weaken the interaction between O and Cr. A clear trend was observed where the binding strength decreases as the metal 3d shell gets more populated leading to a decrease in binding energy with the increase in the Zavg number of the site. This was observed in both, hollow and bridge sites. However, this trend is less pronounced in the HEA than in the pure metal leading to the conclusion that the presence of other atomic elements actually weakens the interaction of O with Cr and Fe and strengthens its interaction with Co while barely affecting the interaction with Ni. The low rate of Ni oxidation is basically caused by a competition

with other metals that even in the HEA environment show higher binding energy to O. Finally, there is good agreement between the experimental UPS and calculated PDOS of the approximated oxidized surface.

Overall, from this study, it was concluded that in CoCrFeNi alloy oxidation is expected to start at Cr-rich sites where Cr_2O_3 will be formed. FeO is also possible; however the creation of these two oxides, particularly Cr_2O_3 , may be slowed down by the presence of the other metals in the vicinity, particularly Fe and Co that showed to be in competition with Cr.

CRediT authorship contribution statement

Frank McKay: Investigation, Validation, Formal analysis, Writing – original draft. Timothy Ismael: Investigation, Software, Writing – original draft. Alexa Robinson: Investigation, Software, Formal analysis. Orhan Kizilkaya: Investigation, Validation, Formal analysis. Phillip T. Sprunger: Supervision, Writing – review & editing. Pedro A Derosa: Supervision, Writing – review & editing.

Declaration of Competing Interest

The authors declare that they have no known competing financial interests or personal relationships that could have appeared to influence the work reported in this paper.

Acknowledgments

This work was supported by the U.S. National Science Foundation under grants #OIA-1541079 (Consortium for Innovation in Manufacturing and Materials) and #OIA1946231 (Louisiana Materials) Design Alliance) and the Louisiana Board of Regents. PD acknowledges the Larson #1 (COES) Professorship made available through the State of Louisiana Board of Regents Support Fund. LONI (Louisiana Optical Network Initiative) computer resources are acknowledged. The skill of D.P Young is gratefully acknowledged for arc melting the sample.

Supplementary materials

Supplementary material associated with this article can be found, in the online version, at doi:10.1016/j.susc.2022.122124.

References

- [1] Y. Brif, M. Thomas, I. Todd, The use of high-entropy alloys in additive manufacturing, Scripta Materialia 99 (2015) 93–96, https://doi.org/10.1016/j. scriptamat.2014.11.037.
- [2] Simonelli, M., et al., A study on the laser spatter and the oxidation reactions during selective laser melting of 316L stainless steel, Al-Si10-Mg, and Ti-6Al-4V. Metallurgical and Materials Transactions A, 2015. 46(9): p. 3842-3851 DOI: 10.1007/s11661-01 5-2882-8.
- [3] J.-P. Kruth, et al., Selective laser melting of iron-based powder, Journal of materials processing technology 149 (1-3) (2004) 616–622, https://doi.org/ 10.1016/j.jmatprotec.2003.11.051.
- [4] Jianian, S., Z. Longjiang, and L. Tiefan, High-temperature oxidation of Fe-Cr alloys in wet oxygen. Oxidation of metals, 1997. 48(3): p. 347-356 DOI: 10.1007/BF01 670507.
- [5] J.R. Davis, Nickel, cobalt, and their alloys, ASM international, 2000.
- [6] M. Warmuzek, Aluminum-silicon casting alloys: an atlas of microfractographs, ASM international, 2004.
- [7] Y. Ye, et al., High-entropy alloy: challenges and prospects, Materials Today 19 (6) (2016) 349–362, https://doi.org/10.1016/j.mattod.2015.11.026.
- [8] M.C. Troparevsky, et al., Beyond atomic sizes and Hume-Rothery rules: understanding and predicting high-entropy alloys, Jom 67 (10) (2015) 2350–2363, https://doi.org/10.1007/s11837-015-1594-2.
- [9] D.B. Miracle, O.N. Senkov, A critical review of high entropy alloys and related concepts, Acta Materialia 122 (2017) 448–511, https://doi.org/10.1016/j. actamat.2016.08.081.
- [10] M. Zhang, et al., Microstructure and mechanical behavior of AlCoCuFeNi highentropy alloy fabricated by selective laser melting, Beijing: SFF (2017) 729–730.

- [11] M. Löbel, et al., Microstructure and wear resistance of AlCoCrFeNiTi high-entropy alloy coatings produced by HVOF, Coatings 7 (9) (2017) 144, https://doi.org/ 10.3300/cost/prz/7000144.
- [12] C.-H. Tsau, W.-L. Wang, Microstructures, hardness and corrosion behaviors of FeCoNiNb0. 5Mo0. 5 and FeCoNiNb high-entropy alloys, Materials 11 (1) (2018) 16, https://doi.org/10.3390/ma11010016.
- [13] N.K. Othman, J. Zhang, D.J. Young, Temperature and water vapour effects on the cyclic oxidation behaviour of Fe–Cr alloys, Corrosion Science 52 (9) (2010) 2827–2836, https://doi.org/10.1016/j.corsci.2010.04.026.
- [14] X. Chen, et al., Microstructure of All. 3CrFeNi eutectic high entropy alloy and oxidation behavior at 1000°C, Journal of Materials Research 32 (11) (2017) 2109–2116, https://doi.org/10.1557/jmr.2017.10.
- [15] B. Gorr, et al., High-temperature oxidation behavior of refractory high-entropy alloys: effect of alloy composition, Oxidation of Metals 88 (3) (2017) 339–349, https://doi.org/10.1007/s11085-016-9696-v.
- [16] S. Middleburgh, et al., Segregation and migration of species in the CrCoFeNi high entropy alloy, Journal of alloys and compounds 599 (2014) 179–182, https://doi. org/10.1016/j.jallcom.2014.01.135.
- [17] M.-H. Tsai, Physical properties of high entropy alloys, Entropy 15 (12) (2013) 5338–5345, https://doi.org/10.3390/e15125338.
- [18] B. Liu, et al., Microstructure and mechanical properties of equimolar FeCoCrNi high entropy alloy prepared via powder extrusion, Intermetallics 75 (2016) 25–30, https://doi.org/10.1016/j.intermet.2016.05.006.
- [19] Kai, W., et al., Air-oxidation of FeCoNiCr-based quinary high-entropy alloys at 700–900 C. Corrosion Science, 2017. 121: p. 116-125 DOI: 10.1016/j.corsci.201 7.02.008
- [20] O. Kizilkaya, et al., High-throughput toroidal grating beamline for photoelectron spectroscopy at CAMD, in: Journal of Physics: Conference Series, IOP Publishing, 2014, https://doi.org/10.1088/1742-6596/493/1/012024.
- [21] K. Paris, M.C., N. Thayer hart, & G. Watson, Atomistix ToolKit Tutorial and Reference Guide, June 2007.
- [22] Perdew, J.P., K. Burke, and M. Ernzerhof, Generalized gradient approximation made simple. Physical review letters, 1996. 77(18): p. 3865 DOI: 10.1103/PhysRevLett 77, 3865
- [23] Y. Zhang, et al., High-entropy alloys with high saturation magnetization, electrical resistivity and malleability, Scientific reports 3 (1) (2013) 1–7.
- [24] Abrams, M.L. and C.D. Sherrill, A comparison of polarized double-zeta basis sets and natural orbitals for full configuration interaction benchmarks. The Journal of chemical physics, 2003. 118(4): p. 1604-1609 DOI: 10.1063/1.1532313.
- [25] Latajka, Z. and S. Scheiner, Improvement of polarized double-zeta basis sets for molecular interactions. Complexes of NH3, OH2, and FH with H+ and Li+. Chemical physics letters, 1984. 105(4): p. 435-439 DOI: 10.1016/0009-2614(84)80058-5.
- [26] Y.-H. Dai, Convergence properties of the BFGS algoritm, SIAM Journal on Optimization 13 (3) (2002) 693–701, https://doi.org/10.1137/ S1052623401383455.
- [27] D.R.S. Saputro, P. Widyaningsih, Limited memory Broyden-Fletcher-Goldfarb-Shanno (L-BFGS) method for the parameter estimation on geographically weighted ordinal logistic regression model (GWOLR), in: AIP Conference Proceedings, AIP Publishing LLC, 2017, https://doi.org/10.1063/1.4995124.
- [28] F. McKay, et al., CoCrFeNi High-Entropy Alloy as an Enhanced Hydrogen Evolution Catalyst in an Acidic Solution, The Journal of Physical Chemistry C 125 (31) (2021) 17008–17018, https://doi.org/10.1021/acs.jpcc.1c03646.
- [29] Qiu, Y., et al., Corrosion characteristics of high entropy alloys. Materials science and technology, 2015. 31(10): p. 1235-1243 DOI: 10.1179/1743284715Y.00000000
- [30] M.C. Biesinger, et al., Resolving surface chemical states in XPS analysis of first row transition metals, oxides and hydroxides: Cr, Mn, Fe, Co and Ni, Applied Surface Science 257 (7) (2011) 2717–2730, https://doi.org/10.1016/j. apsusc.2010.10.051.
- [31] Peak Fitting in XPS. 2021; Available from: http://www.casaxps.com/help_manual/manual_updates/peak_fitting_in_xps.pdf.
- [32] D.A. Shirley, High-resolution X-ray photoemission spectrum of the valence bands of gold, Physical Review B 5 (12) (1972) 4709, https://doi.org/10.1103/ PhysRevB.5.4709.
- [33] S. Doniach, M. Sunjic, Many-electron singularity in X-ray photoemission and X-ray line spectra from metals, Journal of Physics C: Solid State Physics 3 (2) (1970) 285.
- [34] Lambers, E.S., et al., Room-temerature oxidation of Ni (110) at low and atmospheric oxygen pressures. Oxidation of metals, 1996. 45(3): p. 301-321 DOI: 10.1007/BF01 046987.
- [35] W.-X. Li, C. Stampfl, M. Scheffler, Oxygen adsorption on Ag (111): A density-functional theory investigation, Physical Review B 65 (7) (2002), 075407, https://doi.org/10.1103/PhysRevB.65.075407.
- [36] Tanuma, S., C.J. Powell, and D.R. Penn, Calculations of electorn inelastic mean free paths. II. Data for 27 elements over the 50–2000 eV range. Surface and Interface Analysis, 1991. 17(13): p. 911-926 DOI: 10.1002/sia.740171304.
- [37] G. Castro, J. Küppers, Interaction of oxygen with hcp (0001) recrystallized cobalt surfaces, Surface Science 123 (2-3) (1982) 456–470.
- [38] G. Gewinner, et al., Photoemission study of the chromium (111) surface interacting with oxygen, Surface science 78 (2) (1978) 439–458.
- [39] C. Brundle, Oxygen adsorption and thin oxide formation at iron surfaces: An XPS/ UPS study, Surface Science 66 (2) (1977) 581–595.
- [40] H. Conrad, et al., A LEED/UPS study on the interaction of oxygen with a Ni (111) surface, Solid State Communications 17 (4) (1975) 497–500.